Cross-borehole tomography with full-decay spectral time-domain induced polarization for mapping of potential contaminant flow-paths

Author list:

Thue Sylvester Bording* [T] (bording@geo.au.dk)

Gianluca Fiandaca* (gianluca.fiandaca@geo.au.dk)

Pradip Kumar Maurya* (pradip.maurya@geo.au.dk)

Esben Auken* (esben.auken@geo.au.dk)

Anders Vest Christiansen* (anders.vest@geo.au.dk)

Nina Tuxen** (nina.tuxen@regionh.dk)

Knud Erik Strøyberg Klint*** (kek@geo.dk)

Thomas Hauerberg Larsen**** (thla@orbicon.dk)

*HydroGeophysics Group, Department of Geoscience, Aarhus University, Denmark

** Capital Region of Denmark, Denmark

*** GEO, Denmark.

****Orbicon, Denmark

[T] Corresponding author:

Short title: Cross-borehole TDIP tomography

Abstract

Soil contamination from industrial activities is a large problem in urban areas worldwide. Understanding the spreading of contamination to underlying aquifers is crucial to make adequate risk assessments and for designing remediation actions. A large part of the northern hemisphere has quaternary deposits consisting of glacial clayey till. The till often has a complex hydrogeological structure consisting of networks of fractures, sand stringers and sand lenses that each contribute to a transport network for water, free phase and dissolved contaminants. Thus, to determine the possible flow-paths of contaminants, the geology must be described in great detail. Normally, multiple boreholes would be drilled in order to describe the geology, but boreholes alone do not provide the needed resolution to map such sand lenses and their connectivity.

Cross-borehole full-decay time-domain induced polarization (TDIP) is a new tool that allows for quantitatively mapping not only contrasts in bulk resistivity, but also contrasts in spectral IP parameters. We present a feasibility study with synthetic tests and a field application on a clayey moraine environment with embedded sand lenses, with hitherto unseen ground-truth verification. Indeed, the investigated area was above the water table, which allowed for digging out the entire area after the investigation for an unprecedented description of the lens interconnectivity.

The TDIP data were acquired with a full-waveform acquisition at high sampling rate, signal-processed by harmonic denoising, background removal, and de-spiking, and subsequently the full-waveform data were stacked in log-increasing tapered gates (with 7 gates per decade). The resulting TDIP decays, with usable time-gates as early as two milliseconds, were inverted in terms of a re-parameterization of the Cole-Cole model. The inverted models of the field data show a remarkable delineation of the sand lenses/layers at the site, with structure in both the resistivity and the IP parameters matching the results from the ground-truthing. The synthetic examples show that in models both below and above the groundwater table, sand-lenses with thicknesses comparable to the vertical electrode spacing can be well resolved. This suggests that full-decay cross-borehole TDIP is an ideal tool for high-resolution sand-lens imaging.

1. Introduction

Soil and groundwater contamination is a major issue all over the world. This contamination is mainly found in industrialized areas with a high population density, locations of former businesses such as drycleaners, gas stations, chemical factories and landfills. In Denmark alone, more than 10,000 such

contaminated sites are known, while even more remain to be investigated (Danske Regioner 2017). The Denmark region is mainly covered by quaternary deposits, as is a great part of the northern hemisphere, and most of the known contaminated sites in Denmark are on top of clayey moraines. In these moraine environments, the key to understanding subsurface flow-paths is often to understand the geometry of embedded sand layers in the moraine, as the permeability values of the two lithologies can differ by several orders of magnitude. A contaminated site is traditionally characterized by geological descriptions and geochemical data from boreholes, possibly in combination with geophysical borehole logs. This traditional approach does not provide any direct information in the area between the boreholes, so the spatial information is limited to the positions of the boreholes. Pumping tests can be performed to provide information about the connectedness of sand-bodies, but this is only possible below the water table and does not provide any direct information on the geometry of the connected layers.

A possible method of mapping the area between boreholes is by cross-borehole electrical resistivity tomography. While resistivity mapping can be performed by surface measurements, the vertical resolution of these surveys unavoidably decreases with depth. The cross-borehole method maintains an adequate vertical resolution in the entire volume of interest, given a proper borehole separation. The application of cross-borehole resistivity tomography has been demonstrated for various purposes, e.g. characterizing hydrogeological properties of the vadose zone (e.g. Binley et al. 2002, Looms et al. 2008a), monitoring unsaturated flow and transport (e.g. Looms et al. 2008b), quantitative temperature monitoring (e.g. Hermans et al. 2015), and characterizing solute transport processes by saline tracer tests (e.g. Slater et al. 2000, Perri et al. 2012).

Another frequently used cross-borehole geophysical method is ground penetrating radar (GPR), where the EM wave velocity in the vadose zone primarily depends on the moisture content (Topp et al. 1980). Similarly to cross-borehole resistivity mapping, the application of cross-borehole GPR has been used for various purposes, e.g. characterizing soil moisture content (e.g. Paprocki and Alumbaugh 1999), and monitoring infiltration (e.g. Alumbaugh et al. 2000, Looms et al. 2008b, Winship et al. 2006). Data acquisition is very fast with the cross-borehole GPR method compared to electrical methods, and the GPR method works very well in unsaturated, resistive environments. However, in conductive environments, the greater attenuation of the EM signal severely limits the imaging distance between boreholes. Looms et al. (2018), succeeded in mapping sand-lenses in a clayey till by full waveform inversion of cross-borehole GPR data, collected at the same gravel pit as

will be presented here. The main advantage of the resistivity method in comparison to the GPR method, is that the resistivity method also works in fully saturated zones.

The inclusion of IP measurements to resistivity campaigns has started to gain popularity. The IP data add complimentary information to characterize the subsurface (e.g. Kemna et al. 2004), and help to reduce model equivalences (Madsen et al (2017). IP measurements can be carried out in either frequency domain (FD) or in time domain (TD) with different advantages and limitations for the two methodologies; see Maurya et al. (2018b) for a comparison of the different methods. For an in-depth description of the IP phenomenon along with petro-physical models, we refer to other literature (eg. Revil et al. 2017, Okay et al. 2014, Weller et al. 2013).

One of the earliest applications of FD cross-borehole IP was presented by Kemna et al. (2004), where the target was to image hydrocarbon contamination and lithotypes at contaminated sites. The study presents 2D inversion images based on single frequency measurements. Zhao et al. (2014) present a broadband FDIP cross-borehole system, along with methods to correct for inductive and capacitive coupling in the data processing. Their field demonstration was only meant to confirm their correction approach and does not show any cross-borehole tomography. A recent application of cross-borehole TDIP was presented by Binley et al. (2016), where the target was hydrogeological characterization of unconsolidated sediments. They used integral chargeability measurements, disregarding the spectral content of the IP phenomenon.

Full-decay spectral TDIP is an increasingly applied method for surface applications with a multitude of examples: characterization of landfills and contaminated sites (e.g. Gazoty et al. 2012a, Johansson et al. 2015, Wemegah et al. 2017), geological discrimination (e.g. Gazoty et al. 2012b, Rossi et al. 2017), permeability estimation (e.g. Fiandaca et al. 2018b, Maurya et al. 2018a), time-lapse monitoring of CO_2 injection (e.g. Doetsch et al. 2015a, Fiandaca et al. 2015) and active layer dynamics (e.g. Doetsch et al. 2015b). Maurya et al. (2018b) also show that in field applications TDIP can achieve spectral content equivalent to FDIP, but with significantly improved acquisition speed.

In this study, we present the first application of full-decay spectral cross-borehole TDIP for mapping thin sand lenses embedded in clayey moraines. The study was conducted at a test site established in a gravel pit near Hedehusene, Zeeland, Denmark (Kallerup grusgrav, Figure 1a). In the gravel pit, the sand and gravel is overlain by 6-10 m of clayey moraine, with a few, thin sand layers observed (Kessler et al. 2012). The test site was not selected because of the presence of contamination transported in the sand lenses, but because of the great opportunity offered by the gravel pit for

verifying the mapping accuracy: a few weeks after the geophysical data acquisition, the entire site was dug out and geological profiles were constructed. This provides an unprecedented level of ground-truth verification of the geophysical imaging.

2. Methodology

2.1. Data acquisition and processing

The field setup consisted of three boreholes on an 11 m sub-section of a 63 m long surface profile with 1 m electrode spacing (Figure 1b). The borehole electrodes were made by mounting copper-tape on 60 mm PVC-tubes with a vertical spacing of 20 cm. These electrode-tubes were installed in 6'' boreholes, which were backfilled with sand after the installation. The electrode-tubes reached 9.0 m in B1, 10.0 m in B2 and 9.4 m in B3. A photo of an installed electrode-tube can be seen in Figure 2.

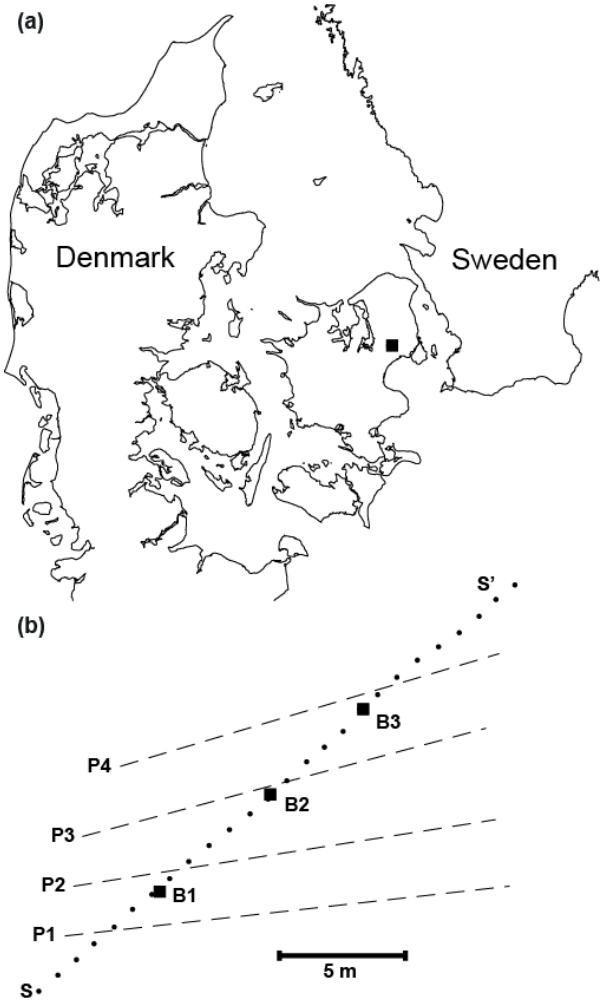

Figure 1: a) Location of the survey area. b) Location of the boreholes (B1-3), the geological profiles (P1-4), and the positions of the electrodes on the surface profile (S-S'). The surface profile extends 40 meters in the direction of S'.

Figure 2: Photo of the installed electrode-tube in B3, showing two unused electrodes above ground. The wires coming out, were connected to the instruments.

The TDIP measurements were performed by a 12 channel ABEM Terrameter LS using a 100 % duty cycle current waveform (Olsson et al. 2015) with 4 seconds on-time. Four different array types were measured as shown in Figure 3:) measurements along the surface profile using mixed gradient/dipole-dipole arrays; b) collinear dipole-dipole single borehole arrays; c) parallel cross-borehole dipole-dipole arrays; d) equatorial cross-borehole dipole-dipole arrays. The different array types are described in detail by e.g. Bing and Greenhalgh (2000). The field campaign took three days, which included installation of boreholes and testing of equipment and measurements, and was carried out in November, 2015. The acquisition time of the TDIP data included in this study was 5-6 hours. In total nearly 6000 quadrupole measurements were collected, evenly distributed between the four array types.

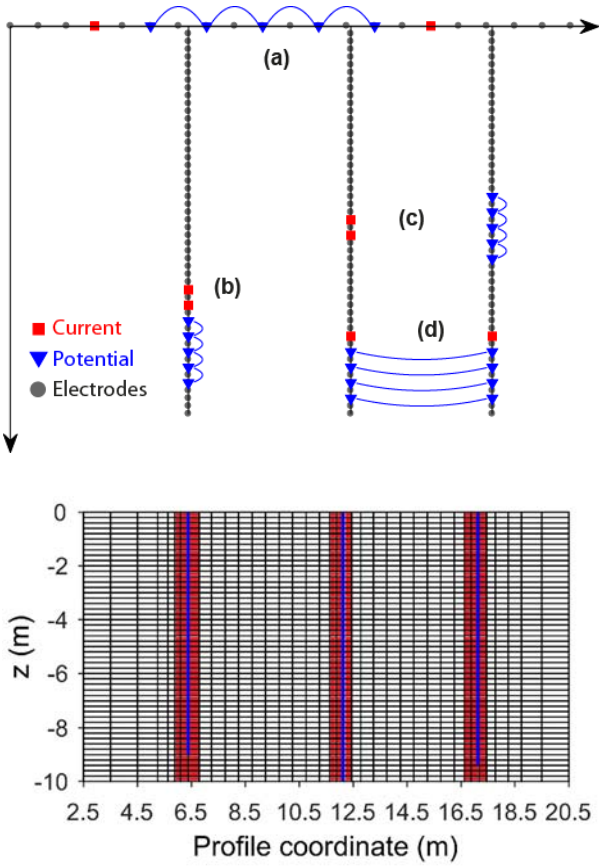

Figure 3. Top: A schematic diagram of the electrode arrays measured: a) surface gradient arrays. b) collinear dipole-dipole single borehole arrays. c) parallel cross-borehole dipole-dipole arrays. d) equatorial dipole-dipole. Bottom: The model mesh used in the inversion of the data. Red cells have no horizontal constraints. Blue lines mark the position of boreholes.

The full-waveform data were signal-processed for harmonic de-noising, drift correction, and spike removal following Olsson et al. (2016), and the signal-processed IP decays were subsequently gated using 25 logarithmically spaced time windows in the range from 0.001s to 3.9 s. The IP decays were manually processed using the Aarhus Workbench software (www.aarhusgeosoftware.dk) where non-regular IP gates or full decays were culled, mainly due to poor electrode contact. Capacitive and inductive coupling in the cables affected the signal at very early times, as seen in Figure 4e-f, where different slopes can be seen in some of the first gates. For this study, data was generally only affected for up to a few ms, and these data were also removed. In general, these effects are dependent on the geometry of the electrodes, the positions and wirings of the cables used, and the resistivity of subsurface, with high resistivities generally resulting in less pronounced effects (Fiandaca 2019).

The initial contact resistances of the borehole electrodes were in the order of a few kΩ, but after a few hours, the contact resistances increased to tens of kΩ due to drainage of the water from the backfilling process. To achieve a better contact resistance, 100 liters of salt water were poured in each

borehole, resulting in a permanent drop of the contact resistance into the kΩ range. Test acquisitions performed before and after the saltwater addition revealed that the IP data quality greatly increased, as shown in Figure 4. The signal processing and the improved contact resistance allowed time gates of the IP decays as early as 2 ms to be used. Almost a full decade of early time gates was gained from the saltwater pouring when compared to test acquisitions prior to the saltwater addition.

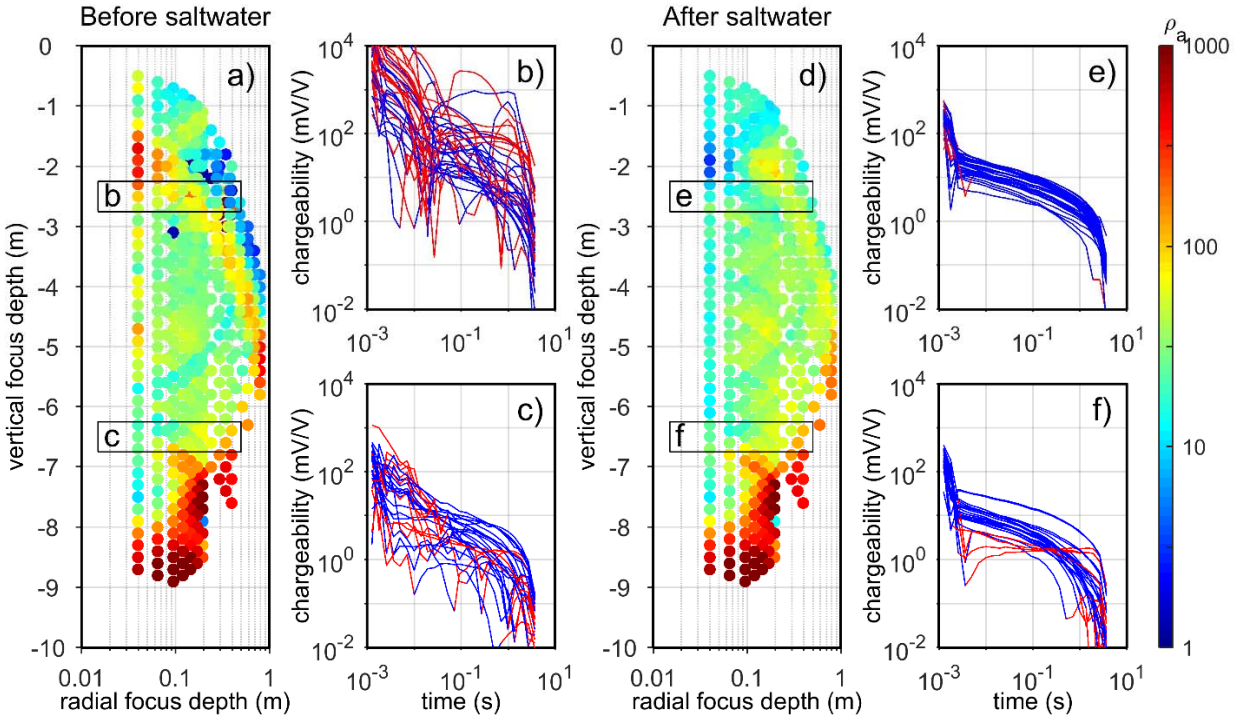

Figure 4: Comparison of IP decay quality before and after saltwater. a) Apparent resistivity pseudo section from single borehole data before saltwater injection. b-c) IP decays from area marked in section a, blue curves are positive, red is negative. d) Apparent resistivity pseudo section from single borehole data after saltwater injection. e-f) IP decays from area marked in section d, blue curves are positive, red are negative.

2.2. Inversion

The collected IP and apparent resistivity data were inverted using AarhusInv (Auken et al. 2014), where the TDIP forward response is calculated in 2.5D using the algorithm described by Fiandaca et al. (2013) modified to allow for buried electrodes. The forward algorithm assumes that the 2D model extends indefinitely in the direction normal to the profile plane, and electrodes are modelled as points. The 2.5D inversion of data measured along 2D profiles has the same kind of benefits and limitations for surface and cross-borehole measurements, when compared to the 3D inversion: the 2.5D inversion is better constrained by the data, because no 3D data coverage is present; 3D structures in the model might be poorly represented in the 2D sections. The measurements with sensitive zones close to the boreholes are affected by the boreholes themselves, where the geology has been replaced by a non-

conductive PVC tube and backfilled sand. This effect has been exacerbated by the addition of saltwater in the boreholes. The borehole effect is a 3D effect, which is not modelled properly in the 2.5D forward algorithm. Consequently, the single-borehole measurements with shortest offset distances (i.e. the measurements more sensitive to the borehole effect) were culled before inversion. These data points are seen as the left-most vertical line in Figure 4d. The capability of the 2.5D inversion in correctly retrieving the geometry of the sand lenses in the field data presented in this study will be discussed in the result section, comparing the imaging results with the excavation results.

The model cell mesh is shown in Figure 3. The layer thicknesses are 20 cm from 0-10 m, and below that, the thicknesses increase logarithmically downwards. Between boreholes, the model widths are 50 cm, with local refinement near boreholes. Outside the boreholes, the model thicknesses increase logarithmically outward. The parameters in each model cell are constrained to the neighboring cells in the vertical and horizontal directions. This stabilizes the inversion and ensures a smooth model. In order to mitigate the borehole effect in the inversion, the horizontal constraints in the immediate vicinity of the boreholes have been removed. This produces sharp lateral transitions around the boreholes, which allows for a good data misfit. The model cells without horizontal constraints are marked with red in Figure 3.

In this study the spectral content of the IP data is parameterized in terms of the maximum imaginary conductivity (MIC) model (Fiandaca et al. 2018a), a re-parameterization of the Cole-Cole model. The Cole-Cole model in the conductivity form is given as (Tarasov and Titov 2013):

$$\sigma^*(f) = \sigma'(f) + i\sigma''(f) = \sigma\left[1 - \frac{m_0}{1-m_0}\left(1 - \frac{1}{1+(i2\pi f\tau_\sigma)^c}\right)\right], \quad (1)$$

where σ^* is the complex conductivity, f is the frequency, $\sigma'$and $\sigma''$are the real and imaginary components, $\sigma = \sigma'(f = 0)$ is the DC conductivity, m_0 is the intrinsic chargeability, τ_σ is the relaxation time, C is the frequency exponent and i is the imaginary unit. In the MIC re-parameterization the intrinsic chargeability m_0 is substituted by the maximum of the imaginary component σ''_{max}, reached at frequency $f = 1/2\pi\tau_\sigma$. The model parameters are thus:

$$\boldsymbol{m_{MIC}} = \{\sigma, \sigma''_{max}, \tau_\sigma, C\}, \quad (2)$$

When compared to the classic Cole-Cole model, in the MIC model weaker correlations exist between the model parameters, and consequently the inversion parameters are better resolved (Fiandaca et al.

2018a). Furthermore, as suggested by Slater and Lesmes (2002), the maximum imaginary conductivity σ''_{max} is a better proxy for lithology than the intrinsic chargeability m_0 of the Cole-Cole model. In the inversion process all parameters are retrieved independently, without constraints between the structural appearances of the four model parameter spaces, i.e. a structure in for example the σ model space is not forced into the σ''_{max} model space. This of course does not mean that the parameters are not correlated, as shown by Fiandaca et al. (2018a) for the MIC parameterization. The model parameters are determined in log-space and bounds are imposed to the parameter ranges, in order to avoid the parameters to get unphysical values (in particular, C is bound to the range 0.1-0.6). The log transformation also ensures parameter positivity.

2.3. Geological settings and excavation

The regional geology consists of limestone basement, with a 15-30 m cover of glacial deposits. These deposits originate from the Weichselian glaciation, which covered the entirety of Zeeland and large parts of the Danish mainland (Houmark-Nielsen 1989). During repeated episodes of advancements and retreats, the glaciers deposited and deformed meltwater sediments and glacial debris, forming a sequence of till planes and other depositional units of varying compositions, sizes, and degrees of deformation. Kessler et al. (2012) studied the till outcrops and sand-lenses in the same gravel pit of our study, and found "sand lenses to occur throughout the till planes in variety of numbers, shapes and geometries". The till is quite heterogeneous in the area, but the general geological framework consists of 6-8 m of clayey to sandy diamict, separated by glacio-fluvial sediments of fine sand to gravel. These glacio-fluvial sediments form sand layers, sheets, stringers, and pockets, with thicknesses ranging from a few centimeters to a few meters and the lateral extent ranging from the sub meter scale to tens of meters. The larger sand bodies are moderately deformed by shear stress, while the smaller deposits show higher degrees of shear stress deformation.

After the collection of the geophysical dataset, the front of the ongoing excavation in the gravel pit eventually reached the test site. The area was then excavated in terraces of 2 m (taller terraces would have collapsed), resulting in the description of four sub-parallel geological profiles. A picture from the excavation is shown in Figure 5, while the positions and orientations of these profiles can be seen in Figure 1b.

Figure 5: Picture from the excavation with the geological profiles P1 and P2 superimposed.

2.4. Synthetic modelling

In order to explore the resolution limits of cross-borehole full-decay spectral TDIP, we constructed a synthetic model based on the geology at the test site. The model is idealized to consist of two geological units, a clayey till unit and a sand unit. From 0-8 m the clayey unit is dominant, separated by a few sand layers with thicknesses of 0.2-0.6 m, (Figure 6). Below 8 m, only the sand unit is present. The model is consistent with the local geology (Kessler et al. 2012) and showcases both layers that are connected or disconnected in the area between boreholes. The use of a 2.5D algorithm in the forward modelling assumes anomalies that continue indefinitely in strike direction perpendicular to the profile.

The parameter values in the geological units were chosen in accordance with laboratory findings, petrophysical relations, and field studies. However, we have limited the maximum parameter contrast between the units to one order of magnitude, in order to make the inversion more challenging (bigger parameter contrasts are easier to retrieve correctly in the inversion process). Specifically, the chosen parameters for the till unit are $\{\sigma = 10\ \mathrm{mS/m}, \sigma''_{max} = 0.1\ \mathrm{mS/m}, \tau_\sigma = 0.01\ \mathrm{s}, C = 0.5\}$ and the parameters for the sand unit are $\{\sigma = 1\ \mathrm{mS/m}, \sigma''_{max} = 0.01\ \mathrm{mS/m}, \tau_\sigma = 0.1\ \mathrm{s}, C = 0.2\}$.

The imaginary conductivity value of the till unit (σ''_{max} = 0.1 mS/m) is in accordance with the values reported for clean clays or sand-clay mixtures presented by Breede et al. (2012) and Okay et al. (2014). A lower value for imaginary conductivity has been used in the sand unit (σ''_{max} = 0.01 mS/m) , considering that the imaginary conductivity is proportional to the surface area per unit volume (Slater et al. 2006). This value is in agreement with values reported for unconsolidated sandy sediments by Slater and Glaser (2003), for sands and gravel by Weller et al. (2013) and for clean sand by Okay et al. (2014). The above listed values were measured in saturated medias, but Ulrich and

Slater (2004) show that the imaginary conductivity is only weakly dependent on the water-saturation, so that their use for unsaturated sediments is justified. The DC conductivity value of 1 mS/m chosen for the sand unit is in the low end for saturated sediments, but not unlikely for unsaturated sands as shown by Titov et al. (2004). Meanwhile, Barfod et al. (2016) show that a DC conductivity of 10 mS/m in tills are not uncommon. The relaxation time for the till unit ($\tau_\sigma = 0.01\ s$) agrees with the value $\tau = \frac{d_0^2}{8D_{(+)}}$ predicted for the Stern layer polarization in clayey materials (Revil and Skold 2011) , using $D_{(+)} = 1.32 \cdot 10^{-9}\ \mathrm{m}^2/s$ for the diffusion coefficient of the counterions of the Stern layer, as in Revil and Skold (2011), and $d_0 = 3.6\ \mu m$ for the grain diameter. The choice of allowing only up to one decade of parameter contrasts between the geological units in the synthetic model resulted in a low relaxation time in the sand unit ($\tau_\sigma = 0.1\ s$). However, this underestimation is not particularly relevant, because of the value of the frequency exponent in the sand unit ($C = 0.2$), which results in a relatively flat IP spectrum. This value of the frequency exponent in the sand unit, as well as the value in the till unit, have been chosen following the inversion results of the field data.

Based on this model, synthetic forward responses were calculated using the same electrode configurations as described section 2.1 and with boreholes at 5 m, 10 m and 15 m positions along the profile axis.

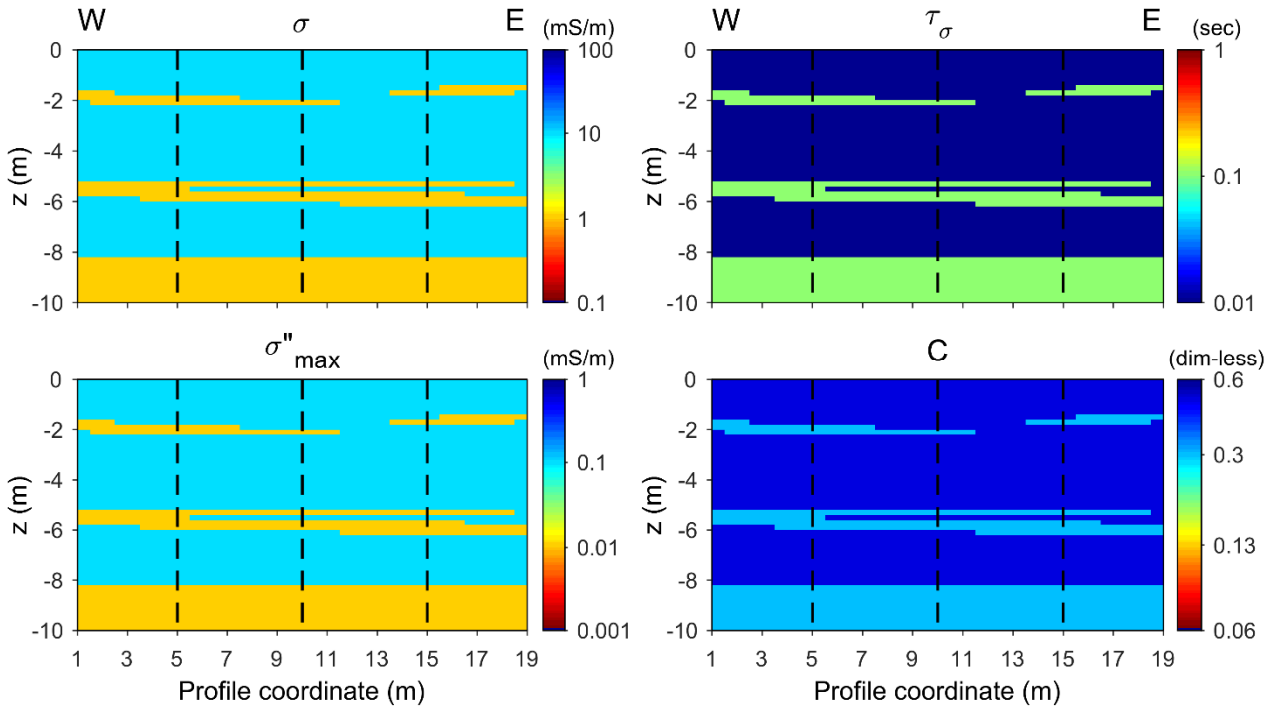

Figure 6: Synthetic model sections, top left: DC conductivity σ, bottom left: maximum imaginary conductivity σ''_{max}, top right: relaxation time τ_σ, and bottom right: frequency exponent C.

Furthermore, in order to emphasize the added value of the IP data, we constructed a second synthetic model, similar to the first for relaxation time, frequency exponent and maximum imaginary conductivity, but with no resistivity contrasts. This model represents a similar geological setting, but with water-saturated sand layers, which often only present a small contrast in DC conductivity in relation to the clayey moraine. The choice of keeping the same values of the IP parameters in the modelling of the saturated medium is justified by the weak dependence of imaginary conductivity on water-saturation (Ulrich and Slater 2004).

For both models the synthetic data were contaminated with random noise, assuming a 1 % standard deviation on the resistivity data and a 10 % standard deviation on the IP data.

3. Results

3.1. Geological model

A new geological profile along the geophysical profile was constructed based on the four geological profiles obtained along the excavation terraces. This profile is shown in Figure 7**Error! Reference source not found.**. Prior to the geophysical data collection, the soil-layer had been removed, which left an exposed sandy to clayey till at the surface. At 2 m below surface, a sand layer with gravel at the base and a varying thickness around ½ m was present. Beneath this layer was again a clayey till,

which became sandier towards the bottom. From around 7 m below surface to the bottom of the profile, a several meters thick sand layer, the Hedeland Fm. was present (i.e. the primary sand source in the gravel pit).

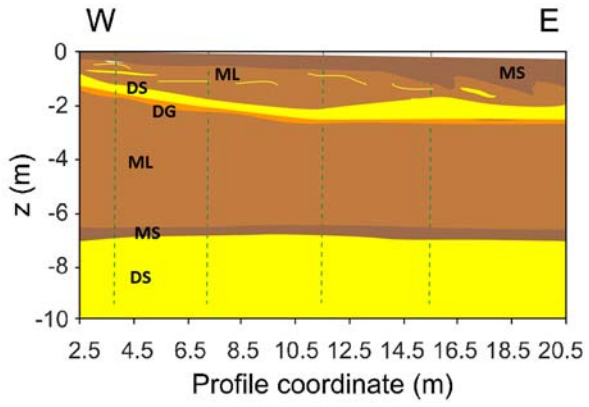

Figure 7: Reconstructed geological profile along the geophysical profile. Green dashed lines indicate the intersections with dug out profiles P1-4. MS: sandy moraine. ML: clayey moraine. DS: sand. DG: gravel

3.2. Field results

The result from the inversion of the data collected at the gravel pit can be seen in Figure 8, with the main geological boundaries derived by the excavation plotted on top with black lines. No *a priori* information, such as the layer boundaries from the excavation, was used in the inversion. The overall structure of the geological model is exceptionally delineated by the inversion, especially in the DC conductivity and the maximum imaginary conductivity sections. The thin sand layer around a depth of 2 m is clearly resolved as a low conductivity anomaly in the DC conductivity section and as a low imaginary conductivity layer in the σ''_{max} section. The frequency exponent (C) section also shows an anomaly corresponding to the thin sand layer, but less defined. The relaxation time section indicates no clear boundaries of the thin sand layer. The good agreement between the inversion models and the ground-truth verification fully justifies, *a posteriori*, the use of the 2.5D algorithm in the forward modelling.

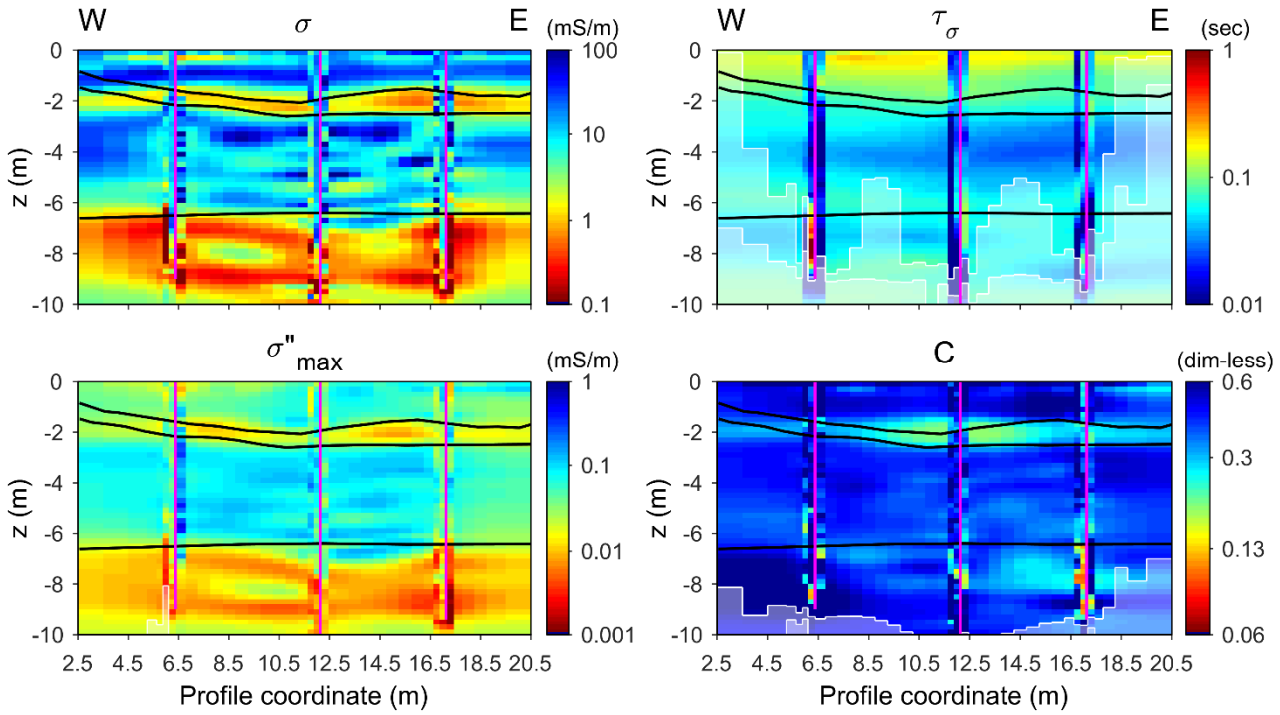

Figure 8: Inversion of collected data. Model sections, top left: DC conductivity σ, bottom left: maximum imaginary conductivity σ''_{max}, top right: relaxation time τ_σ, and bottom right: frequency exponent C.

3.3. Synthetic results

The inversion result from the first synthetic model is shown in Figure 9. The DC conductivity and maximum imaginary conductivity sections both accurately reproduce the structure of the model as well as actual parameter values. The relaxation time and frequency exponent sections reproduce the general structure between the boreholes, but reproduce the actual parameter values to a lesser extent, especially below and outside the boreholes. The inversion result of the second synthetic model, with no DC conductivity contrast, is presented in Figure 10. Here the inversion captures the structure of the model in the maximum imaginary conductivity and frequency exponent sections. In the relaxation time section, the thin sand layers are not resolved, but the sandy base of the model is resolved. On the contrary, in the frequency exponent section the layering is well resolved. Clearly, a resistivity-only dataset would not provide any insight to the structure of this model.

Moreover, these two examples show that layers even thinner than the ones excavated in the field examples, with thickness down to a few tens of centimeters, can be imaged with cross-borehole spectral TDIP measurements.

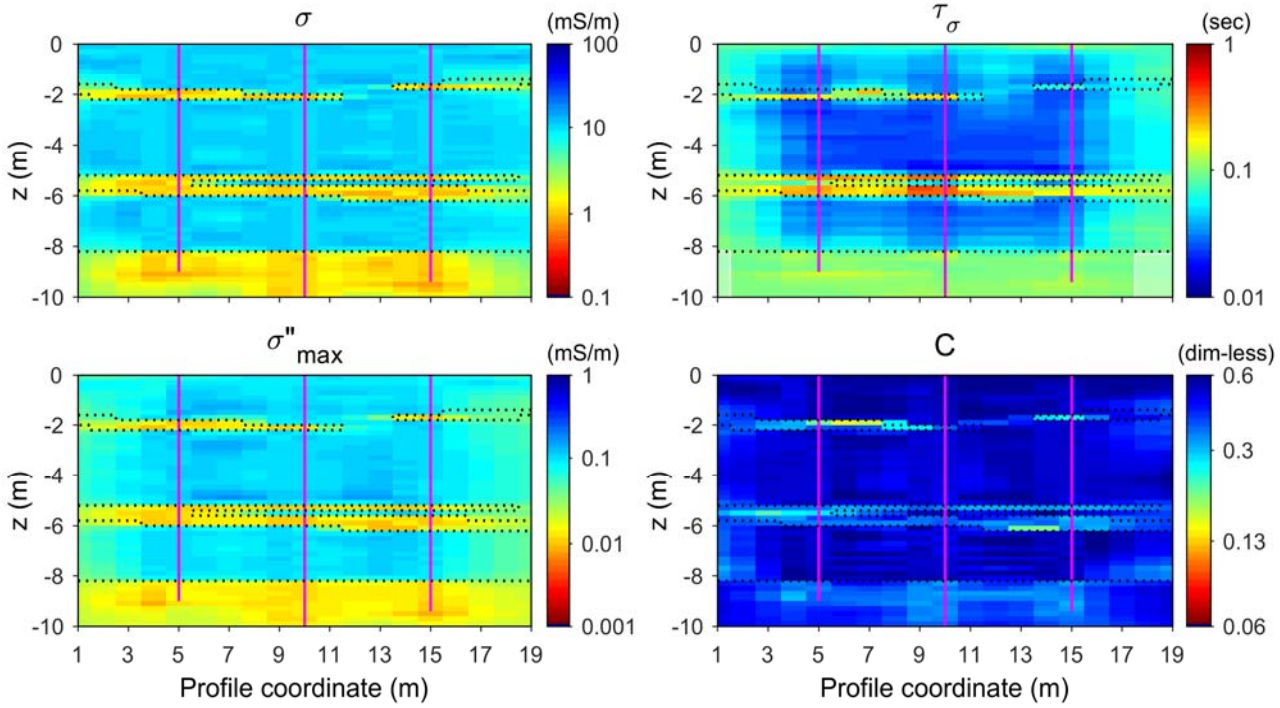

Figure 9: Inversion of synthetic data. Model sections, top left: DC conductivity σ, bottom left: maximum imaginary conductivity σ''_{max}, top right: relaxation time τ_σ, and bottom right: frequency exponent C. The true model boundaries are shown with dotted lines.

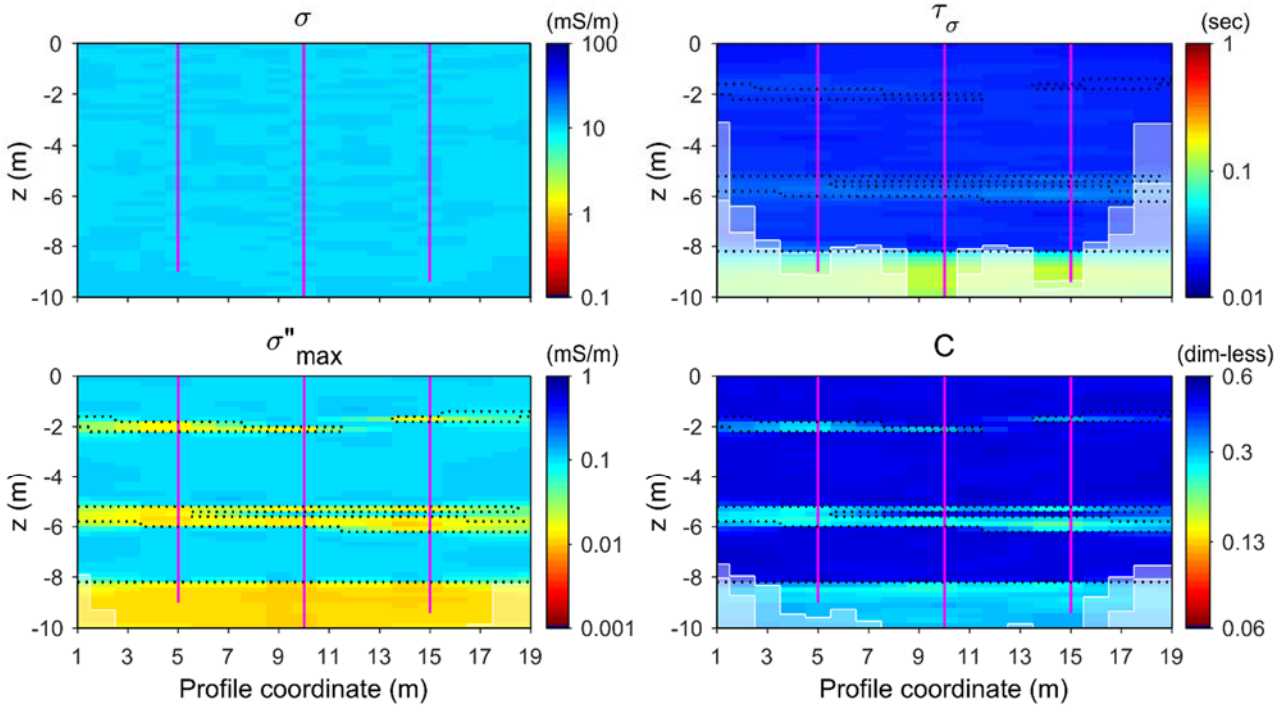

Figure 10: Inversion of synthetic data, but with no contrast in DC conductivity. Model sections, top left: DC conductivity σ, bottom left: maximum imaginary conductivity σ''_{max}, top right: relaxation time τ_σ, and bottom right: frequency exponent C. The true model boundaries are shown with dotted lines.

4. Discussion

This study shows the value of cross-borehole TDIP for mapping sand lenses in in glacial till settings above the groundwater table. The field results show that the sand-lens structure found in the excavation was very well mapped in both the DC conductivity and maximum imaginary conductivity sections, which corroborate each other in the interpretation. However, the contrast in DC conductivity in our field test are large enough for identifying the sand lens solely by resistivity data. The real benefit of cross-borehole TDIP comes when the resistivity contrasts are small, which often is the case below the water table. Moving below the water table, the imaginary conductivity only changes slightly, as it is only weakly dependent on water-saturation (e.g. Ulrich and Slater 2004, Breede et al. 2012) and water conductivity (e.g. Slater and Glaser 2003). This will ensure a significant parameter contrast in imaginary conductivity also in saturated media, the contrast depending mainly on the clay content (e.g. Okay et al. 2014). This potential of the IP method for mapping sand/clay structures below the water table has been evaluated in this study through synthetic modelling, but field verifications are needed for fully establishing the IP method for mapping potential flow-paths of contamination below water table. However, it is important to note that the approach presented in Maurya et al. (2018a) and Fiandaca et al. (2018b) for mapping intrinsic permeability, or its counterpart the hydraulic permeability, could be used in cross-borehole imaging in saturated media, opening the way for quantitative prediction of water flow and contaminant transport. Above the water table, mapping permeability is more difficult because a good estimate of saturation with depth is needed.

The scope of the sand-lens mapping in glacial tills is to identify potential flow-paths for contamination. However, the presence of contaminants, such as hydrocarbons and their degradation products, may alter the IP signal (e.g. Orozco et al. 2012, Johansson et al. 2015). The IP effect of contamination is usually significant only when the concentrations of contaminants are close to the saturation point (e.g. above 1000 mg l^{-1} for BTEX in Orozco et al. (2012)), which usually happens only in the close vicinity of the contamination source. For instance, in Maurya et al. (2018a), TDIP measured in a highly contaminated site was not affected significantly by contamination, and it was possible to retrieve permeability estimates from IP. The underlying assumption in this study is that, when mapping sand lenses in contaminated areas, the contaminant concentrations are low enough to not have a significant IP effect.

The main challenge in this study was the high contact resistances in the boreholes, which negatively affected the IP data quality. The contact resistance problem was solved in a manner that unfortunately resulted in a significant borehole effect. The efforts made to mitigate this effect involved removing affected data and removing horizontal constraints near boreholes, and, while successful, this resulted in totally unresolved parameters near the boreholes. The contact resistance issue and borehole effects in general can potentially be reduced by changing the way the electrodes are installed. The backfilled sand may be mixed with additives (e.g. starch or polymer-based gels) that decrease the contact resistance and mimic the background resistivity, and the low mobility of the starch/gel additives would avoid the draining of the backfilling. The installation of borehole electrodes may also be performed by direct push methods, fully avoiding the need for subsequent backfilling. These recommendations are similar to Nimmer et al. (2008)'s recommendations on how to limit 3D effects in 2D imaging.

As shown in this and previous studies, the IP cross-borehole tomography is versatile method that can be applied in a variety of settings, however dependent on the setting and mapping target, other geophysical cross-borehole approaches may be better suited.

5. Conclusion

Resistivity and full-waveform TDIP measurements were carried out in a cross-borehole setup at a test-site to test the feasibility for mapping possible flow paths of contaminants in thin sand layers. The collected resistivity and IP data were inverted in terms of the MIC model. Following the field campaign, the entire test-site was dug out, providing a hitherto unseen ground-truth verification.

With the above-mentioned setup, processing, and inversion methods it was possible to obtain an exceptionally good delineation of the sand lenses/layers at the site and a near perfect match with the section from the geological excavation. The delineation is clearly visible in both the DC conductivity and maximum imaginary conductivity sections.

With a synthetic example, we show that sand-lenses down to a few tens of centimeters can be well resolved. Furthermore, with another synthetic example, we show that in geological settings with little to no contrast in resistivity between water-saturated sand and clay, sand-lenses can still be resolved in the maximum imaginary conductivity section.

Consequently, cross-hole TDIP imaging is very promising tool for characterizing sand layers serving as possible flow paths of contaminants in clayey sediments. With this tool, high-resolution images of

lenses and connectivity can be obtained, with a reduced need for drillings and significantly decreased cost of site characterization.

Acknowledgement

This work was funded by The Capital Region of Denmark.

References

Alumbaugh, D., Paprocki, L., Brainard, J. & Rautman, C. Year. Monitoring infiltration within the vadose zone using cross borehole ground penetrating radar. Conference Monitoring infiltration within the vadose zone using cross borehole ground penetrating radar, 273-281.

Auken, E., Christiansen, A.V., Kirkegaard, C., Fiandaca, G., Schamper, C., Behroozmand, A.A., Binley, A., Nielsen, E., Effersø, F., Christensen, N.B., Sørensen, K.I., Foged, N. & Vignoli, G. 2014. An overview of a highly versatile forward and stable inverse algorithm for airborne, ground-based and borehole electromagnetic and electric data. *Explor. Geophys*, 1-13.

Barfod, A.A.S., Møller, I. & Christiansen, A.V. 2016. Compiling a national resistivity atlas of Denmark based on airborne and ground-based transient electromagnetic data. *Journal of Applied Geophysics* **134**, 199-209.

Bing, Z. & Greenhalgh, S.A. 2000. Cross-hole resistivity tomography using different electrode configurations. *Geophysical Prospecting* **48**, 887-912.

Binley, A., Cassiani, G., Middleton, R. & Winship, P. 2002. Vadose zone flow model parameterisation using cross-borehole radar and resistivity imaging. *Journal of Hydrology* **267**, 147-159.

Binley, A., Keery, J., Slater, L., Barrash, W. & Cardiff, M. 2016. The hydrogeologic information in cross-borehole complex conductivity data from an unconsolidated conglomeratic sedimentary aquifer. *Geophysics* **81**, E409-E421.

Breede, K., Kemna, A., Esser, O., Zimmermann, E., Vereecken, H. & Huisman, J.A. 2012. Spectral induced polarization measurements on variably saturated sand-clay mixtures. *Near Surface Geophysics* **2012**, 479-490.

Danske Regioner. 2017. Regionernes arbejde med jordforurening, https://www.regioner.dk/media/10099/regionernes_arbejde_med_jordforurening_-_aarsrapport_2018.pdf. pp. 44.

Doetsch, J., Fiandaca, G., Auken, E., Christiansen, A.V., Cahill, A.G. & Jacobsen, J.D. 2015a. Field scale time-domain spectral induced polarization monitoring of geochemical changes induced by injected CO_2 in a shallow aquifer. *Geophysics* **80**, WA113-WA126.

Doetsch, J., Ingemann-Nielsen, T., Christiansen, A.V., Fiandaca, G., Auken, E. & Elberling, B. 2015b. Direct current (DC) resistivity and induced polarization (IP) monitoring of active layer dynamics at high temporal resolution. *Cold Regions Science and Technology* **119**, 16-28.

Fiandaca, G. 2019. Induction-free acquisition range in spectral time- and frequency-domain induced polarization at field scale. *Geophysical Journal International*, in press, 10.1093/gji/ggy409.

Fiandaca, G., Doetsch, J., Vignoli, G. & Auken, E. 2015. Generalized focusing of time-lapse changes with applications to direct current and time-domain induced polarization inversions. *Geophysical Journal International* **203**, 1101-1112.

Fiandaca, G., Madsen, L.M. & Maurya, P.K. 2018a. Re-parameterizations of the Cole-Cole model for improved spectral inversion of induced polarization data. *Near Surface Geophysics* **16**, 385-399.

Fiandaca, G., Maurya, P.K., Balbarini, N., Hördt, A., Christiansen, A.V., Foged, N., Bjerg, P.L. & Auken, E. 2018b. Permeability Estimation Directly From Logging-While-Drilling Induced Polarization Data. *Water Resources Research* **54**, 2851-2870.

Fiandaca, G., Ramm, J., Binley, A., Gazoty, A., Christiansen, A.V. & Auken, E. 2013. Resolving spectral information from time domain induced polarization data through 2-D inversion. *Geophysical Journal International* **192**, 631-646.

Gazoty, A., Fiandaca, G., Pedersen, J., Auken, E. & Christiansen, A.V. 2012a. Mapping of landfills using time-domain spectral induced polarization data: The Eskelund case study. *Near Surface Geophysics* **10**, 575-586.

Gazoty, A., Fiandaca, G., Pedersen, J., Auken, E., Christiansen, A.V. & Pedersen, J.K. 2012b. Application of time domain induced polarization to the mapping of lithotypes in a landfill site. *HESS* **16**, 1793-1804.

Hermans, T., Wildemeersch, S., Jamin, P., Orban, P., Brouyère, S., Dassargues, A. & Nguyen, F. 2015. Quantitative temperature monitoring of a heat tracing experiment using cross-borehole ERT. *Geothermics* **53**, 14-26.

Houmark-Nielsen, M. 1989. The last interglacial-glacial cycle in Denmark. *Quaternary International* **3-4**, 31-39.

Johansson, S., Fiandaca, G. & Dahlin, T. 2015. Influence of non-aqueous phase liquid configuration on induced polarization parameters: Conceptual models applied to a time-domain field case study. *Journal of Applied Geophysics* **123**, 295-309.

Kemna, A., Binley, A. & Slater, L. 2004. Crosshole IP imaging for engineering and environmental applications. *Geophysics* **69**, 97-107.

Kessler, T.C., Klint, K.E.S., Nilsson, B. & Bjerg, P.L. 2012. Characterization of sand lenses embedded in tills. *Quaternary Science Reviews* **53**, 55-71.

Looms, M.C., Binley, A., Jensen, K.H., Nielsen, L. & Hansen, T.M. 2008a. Identifying unsaturated hydraulic parameters using an integrated data fusion approach on cross-borehole geophysical data. *Vadose Zone Journal* **7**, 238-248.

Looms, M.C., Jensen, K.H., Binley, A. & Nielsen, L. 2008b. Monitoring unsaturated flow and transport using cross-borehole geophysical methods. *Vadose Zone Journal* **7**, 227-237.

Looms, M.C., Klotzsche, A., Kruk, J.v.d., Larsen, T.H., Edsen, A., Tuxen, N., Hamburger, N., Keskinen, J. & Nielsen, L. 2018. Mapping sand layers in clayey till using crosshole ground-penetrating radar. *GEOPHYSICS* **83**, A21-A26.

Madsen, L., Fiandaca, G., Christiansen, A. & Auken, E. 2017. Resolution of well-known resistivity equivalences by inclusion of time-domain induced polarization data. *GEOPHYSICS* **83**, E47-E54.

Maurya, P.K., Balbarini, N., Møller, I., Rønde, V., Christiansen, A.V., Bjerg, P.L., Auken, E. & Fiandaca, G. 2018a. Subsurface imaging of water electrical conductivity, hydraulic permeability and lithology at contaminated sites by induced polarization. *Geophysical Journal International*, 770 - 785.

Maurya, P.K., Fiandaca, G., Christiansen, A.V. & Auken, E. 2018b. Field-scale comparison of frequency- and time-domain spectral induced polarization. *Geophysical Journal International* **214**, 1441-1466.

Nimmer, R.E., Osiensky, J.L., Binley, A.M. & Williams, B.C. 2008. Three-dimensional effects causing artifacts in two-dimensional, cross-borehole, electrical imaging. *Journal of Hydrology* **359**, 59-70.

Okay, G., Leroy, P., Ghorbani, A., Cosenza, P., Camerlynck, C., Cabrera, J., Florsch, N. & Revil, A. 2014. Spectral induced polarization of clay-sand mixtures: Experiments and modeling. *Geophysics* **79**, E353-E375.

Olsson, P.-I., Fiandaca, G., Larsen, J.J., Dahlin, T. & Auken, E. 2016. Doubling the spectrum of time-domain induced polarization by harmonic de-noising, drift correction, spike removal, tapered gating and data uncertainty estimation. *Geophysical Journal International* **207**, 774-784.

Olsson, P.I., Dahlin, T., Fiandaca, G. & Auken, E. 2015. Measuring time-domain spectral induced polarization in the on-time:decreasing acquisition time and increasing signal-to-noise ratio. *Journal of Applied Geophysics* **2015**, 6.

Orozco, A.F., Kemna, A., Oberdörster, C., Zschornack, L., Leven, C., Dietrich, P. & Weiss, H. 2012. Delineation of subsurface hydrocarbon contamination at a former hydrogenation plant using spectral induced polarization imaging. *Journal of Contaminant Hydrology* **136-137**, 131-144.

Paprocki, L. & Alumbaugh, D. Year. An investigation of cross-borehole ground penetrating radar measurements for characterizing the 2D moisture content distribution in the vadose zone. Conference An investigation of cross-borehole ground penetrating radar measurements for characterizing the 2D moisture content distribution in the vadose zone, 583-592.

Perri, M.T., Cassiani, G., Gervasio, I., Deiana, R. & Binley, A. 2012. A saline tracer test monitored via both surface and cross-borehole electrical resistivity tomography: Comparison of time-lapse results. *Journal of Applied Geophysics* **79**, 6-16.

Revil, A., Coperey, A., Shao, Z., Florsch, N., Fabricius, I.L., Deng, Y., Delsman, J.R., Pauw, P.S., Karaoulis, M., de Louw, P.G.B., van Baaren, E.S., Dabekaussen, W., Menkovic, A. & Gunnink, J.L. 2017. Complex conductivity of soils. *Water Resources Research* **53**, 7121-7147.

Revil, A. & Skold, M. 2011. Salinity dependence of spectral induced polarization in sands and sandstones. *Geophysical Journal International* **187**, 813-824.

Rossi, M., Olsson, P.I., Johanson, S., Fiandaca, G., Bergdahl, D.P. & Dahlin, T. 2017. Mapping geological structures in bedrock via large-scale direct current resistivity and time-domain induced polarization tomography. *Near Surface Geophysics* **15**, 657-667.

Slater, L., Binley, A.M., Daily, W. & Johnson, R. 2000. Cross-hole electrical imaging of a controlled saline tracer injection. *Journal of Applied Geophysics* **44**, 85-102.

Slater, L., Ntarlagiannis, D. & Wishart, D. 2006. On the relationship between induced polarization and surface area in metal-sand and clay-sand mixtures. *Geophysics* **71**, A1-A5.

Slater, L.D. & Glaser, D.R. 2003. Controls on induced polarization in sandy unconsolidated sediments and application to aquifer characterization. *Geophysics* **68**, 1547-1558.

Slater, L.D. & Lesmes, D. 2002. IP interpretation in environmental investigations. *Geophysics* **67**, 77-88.

Tarasov, A. & Titov, K. 2013. On the use of the Cole–Cole equations in spectral induced polarization. *Geophysical Journal International* **195**, 352-356.

Titov, K., Kemna, A., Tarasov, A. & Vereecken, H. 2004. Induced polarization of unsaturated sands determined through time domain measurements. *Vadose Zone Journal* **3**, 1160-1168.

Topp, G.C., Davis, J. & Annan, A.P. 1980. Electromagnetic determination of soil water content: Measurements in coaxial transmission lines. *Water resources research* **16**, 574-582.

Ulrich, C. & Slater, L.D. 2004. Induced polarization measurements on unsaturated, unconsolidated sands. *Geophysics* **69**, 762-771.

Weller, A., Slater, L. & Nordsiek, S. 2013. On the relationship between induced polarization and surface conductivity: Implications for petrophysical interpretation of electrical measurements. *GEOPHYSICS* **78**, D315-D325.

Wemegah, D.D., Fiandaca, G., Auken, E., Menyeh, A. & Danuor, S.K. 2017. Spectral time-domain induced polarisation and magnetic surveying− an efficient tool for characterisation of solid waste deposits in developing countries. *Near Surface Geophysics* **15**, 75-84.

Winship, P., Binley, A. & Gomez, D. 2006. Flow and transport in the unsaturated Sherwood Sandstone: characterization using cross-borehole geophysical methods. *Geological Society, London, Special Publications* **263**, 219-231.

Zhao, Y., Zimmermann, E., Huisman, J.A., Treichel, A., Wolters, B., van Waasen, S. & Kemna, A. 2014. Phase correction of electromagnetic coupling effects in cross-borehole EIT measurements. *Measurement science and technology* **26**, 015801.